Correlative theoretical and experimental investigation of the formation of $AlYB_{14}$ and competing phases

Oliver Hunold, Yen-Ting Chen, Denis Music, Per O. Å. Persson, Daniel Primetzhofer, Moritz to Baben, Jan-Ole Achenbach, Philipp Keuter, and Jochen M. Schneider

Citation: Journal of Applied Physics **119**, 085307 (2016); doi: 10.1063/1.4942664
View online: https://doi.org/10.1063/1.4942664
View Table of Contents: http://aip.scitation.org/toc/jap/119/8
Published by the American Institute of Physics

JOURNAL OF APPLIED PHYSICS **119**, 085307 (2016)

Correlative theoretical and experimental investigation of the formation of $AlYB_{14}$ and competing phases

Oliver Hunold,[1,a)] Yen-Ting Chen,[1] Denis Music,[1] Per O. Å. Persson,[2] Daniel Primetzhofer,[3] Moritz to Baben,[1] Jan-Ole Achenbach,[1] Philipp Keuter,[1] and Jochen M. Schneider[1]
[1]*Materials Chemistry, RWTH Aachen University, Kopernikusstr. 10, D-52074 Aachen, Germany*
[2]*Department of Physics, Chemistry and Biology (IFM), Linköping University, S-58183 Linköping, Sweden*
[3]*Department of Physics and Astronomy, Uppsala University, Lägerhyddsvägen 1, S-75120 Uppsala, Sweden*

(Received 11 November 2015; accepted 11 February 2016; published online 25 February 2016)

The phase formation in the boron-rich section of the Al-Y-B system has been explored by a correlative theoretical and experimental research approach. The structure of coatings deposited via high power pulsed magnetron sputtering from a compound target was studied using elastic recoil detection analysis, electron energy loss spectroscopy spectrum imaging, as well as X-ray and electron diffraction data. The formation of $AlYB_{14}$ together with the $(Y,Al)B_6$ impurity phase, containing 1.8 at. % less B than $AlYB_{14}$, was observed at a growth temperature of 800 °C and hence 600 °C below the bulk synthesis temperature. Based on quantum mechanical calculations, we infer that minute compositional variations within the film may be responsible for the formation of both icosahedrally bonded $AlYB_{14}$ and cubic $(Y,Al)B_6$ phases. These findings are relevant for synthesis attempts of all boron rich icosahedrally bonded compounds with the space group: *Imma* that form ternary phases at similar compositions. © *2016 AIP Publishing LLC*.
[http://dx.doi.org/10.1063/1.4942664]

I. INTRODUCTION

Icosahedral boron-rich solids exhibit outstanding physical properties, such as high hardness at low density,[1–4] high wear resistance,[5] high stiffness,[6–8] extremely high melting point,[1] thermal stability,[2] exceptional tolerance against radiation damage,[2] and high Seebeck coefficient.[9–11] Such properties render these materials suitable for many applications, e.g., neutron absorber in nuclear reactors,[9] energy conversion,[2,9,11] and protective coatings.[1,2,12,13] These properties are enabled by the presence of a B icosahedra network in these solids.

The formation of these materials in bulk form relies on processing under high temperature and/or high pressure conditions.[1,12,14] Controlling the incorporation of impurities and the formation of competing phases are key challenges to be addressed during synthesis;[15] e.g., the occurrence of YB_6 during synthesis of B_{14}-phases has been reported.[10] The influence of such phases, with similar chemical composition to B_{14}-phases, on the synthesis of B_{14}-phases has not been investigated in a systematic way. Besides synthesis in bulk form[16,17] also thin film synthesis of icosahedral boron-rich solids[15,18] has been reported. The icosahedrally bonded borides should not be confused with other icosahedral phases such as quasicrystals. The following XZB_{14} compounds where X and Z are metal atoms (space group: *Imma*), see Fig. 1, have been synthesized in bulk form: $AlYB_{14}$,[10,16] $AlMgB_{14}$,[17,19] $AlLiB_{14}$,[17,20] $NaAlB_{14}$,[21] Mg_2B_{14},[22] $LnAlB_{14}$ (Ln = Tb, Dy, Ho, Er, Yb, Lu),[23] and $AlMgB_{14}$-TiB_2.[24,25] The bulk synthesis of crystalline $AlMgB_{14}$[17] and $AlYB_{14}$[16] has been reported at temperatures above 1400 °C, and the crystallographic properties of $Al_{0.5–0.8}Mg_{1.0–1.1}B_{14}$[19] and $Al_{0.71}Y_{0.62}B_{14}$[16] are presented by Matkovich and Economy and Korsukova *et al.*, respectively.

Attempts to grow $AlMgB_{14}$ thin films by pulsed laser deposition[15] and magnetron sputtering (MS)[26] both at temperatures of 600 °C resulted in the formation of X-ray amorphous structures. So far, only post-annealing of films with the composition of $AlMgB_{14}$ resulted in the formation of crystalline $AlMgB_{14}$ at temperatures of 1000 °C.[15] Tian *et al.* observed three distinct peaks at 13.85°, 27.89°, and 42.37° corresponding to (011), (022), and (033) planes, respectively.[15] For Al-Y-B, direct synthesis of crystalline $AlYB_{14}$ thin films at a substrate temperature of $T_S = 800$ °C was reported by Kölpin *et al.*[18] In that work, a combination of direct current (DC) and radio frequency (RF)—MS was used, but the mechanisms which trigger the growth of crystalline $AlYB_{14}$ remain unclear.[18] The phase formation was reported based on the presence of 6 diffraction peaks which are consistent with the $AlYB_{14}$ structure: 25.374°, 35.300°, 37.270°, 40.346°, 41.949°, and 42.059° corresponding to (121), (220), (132), (123), (231), and (033) planes, respectively.[18] Yan *et al.*[27] reported the formation of $AlMgB_{14}$ nanocrystals in an amorphous Al-Mg-B matrix in the as deposited state at a substrate temperature of 200 °C based on diffraction data reported in 2013.[28] Yan *et al.* utilized an AlMg compound target which was operated in DC mode and two B targets which were according to the authors sputtered using 350 kHz pulses.[28] This is the first report on the direct synthesis of crystalline $AlMgB_{14}$ at a temperature of 200 °C.[28] No discussion of the physical mechanism enabling the synthesis at these very low growth temperatures is given.[28] The diffraction peak at 42.3° was associated by the authors with the formation of the $AlMgB_{14}$ structure.[28] This

a)Author to whom correspondence should be addressed. Electronic mail: hunold@mch.rwth-aachen.de

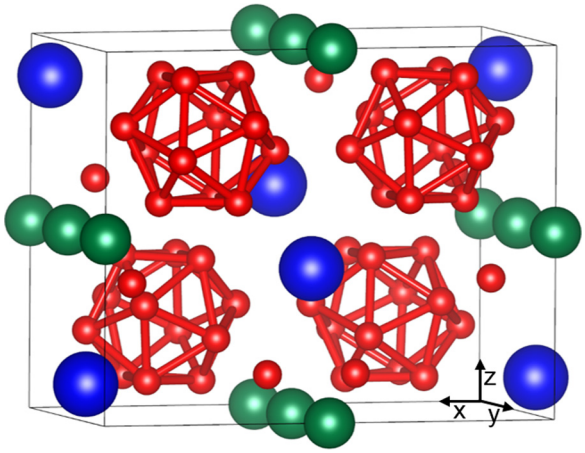

FIG. 1. Unit cell of XZB_{14} structure (space group: *Imma*), where small and big spheres represent B and metal atoms, X and Z, respectively.

peak is shifted by 0.3° with respect to (213) position given in JCPDS No. 75-1262.[28,29] Furthermore, Yan *et al.*[28] present selected area electron diffraction (SAED) data showing a diffuse diffraction ring which is also assigned to (213). For an Al-Mg-B-Ti thin film containing 17.3 at. % Ti only one peak can be found in the diffractogram.[28] This peak position is consistent with the $AlMgB_{14}$ structure. No shift with respect to JCPDS No. 75-1262[29] can be seen.[28] No SAED is presented for the thin film containing 17.3 at. % Ti, though. The authors assign the single diffraction peak to textured growth of the $AlMgB_{14}$-phase.[28] However, if nanocrystals are dispersed in an amorphous matrix as suggested by Yan *et al.*[28] an identical orientation of all nanocrystals appears rather unlikely. Hence, multiple diffraction peaks from the $AlMgB_{14}$-phase should be expected. Hence, both of the above discussed diffraction data sets[28] leave room for alternative phase formation scenarios as presented by the authors.[28]

During PVD growth from compound targets the film composition may deviate from the target composition[30,31] which may cause the formation of competing phases. Possible competing phases are YB_{12},[32] YB_6,[33] $AlYB_{14}$,[16] AlB_{12},[34] and AlB_{10}.[35] Considering additional O incorporation in the growing film from residual gas[36] or as a consequence of post growth atmosphere exposure,[37] even more phases have to be considered: Al_2O_3,[38] Y_2O_3,[39] and $YAlO_3$.[40] The diffraction data (Cu K_α) of the previously listed phases are shown in Fig. 2. It is immediately evident that multiple peak overlaps occur and that a positive phase identification only based on X-ray diffraction (XRD) in this material system is challenging.

It was discussed above that for the synthesis of crystalline $AlYB_{14}$ thin films, a substrate temperature of 800 °C was required.[18] To allow for deposition onto technologically relevant substrate materials for the application as cutting and forming tools, the synthesis temperature of crystalline icosahedrally bonded borides has to be decreased.

It has been reported that by utilizing high power pulsed MS (HPPMS), the deposition temperature can be lowered as compared to DC sputter deposited thin films. HPPMS is a prolific provider of ions formed from the sputter gas as well as from the sputtered and hence film forming species.[41,42] These ions have been reported to enhance the adatom

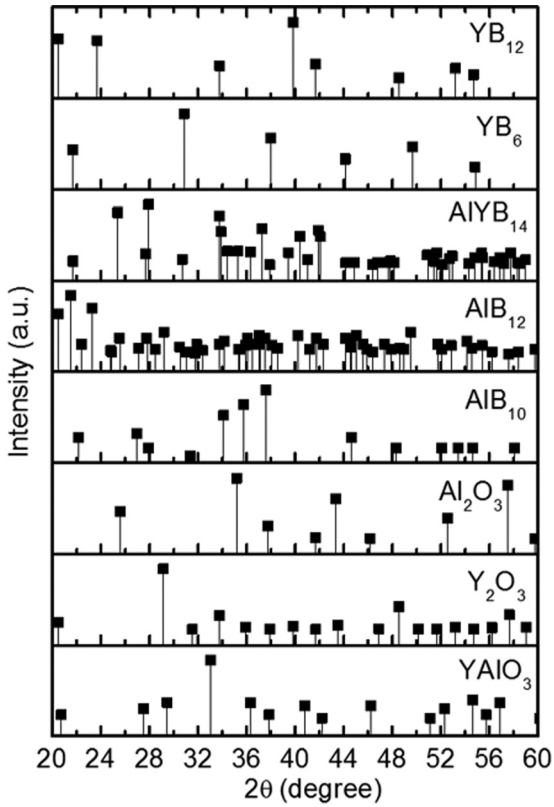

FIG. 2. Peak positions of YB_{12},[32] YB_6,[33] $AlYB_{14}$,[16] AlB_{12},[34] AlB_{10},[35] Al_2O_3,[38] Y_2O_3,[39] and $YAlO_3$.[40]

mobility resulting in a reduction of the synthesis temperature for Mo_2BC from 900 °C (Ref. 43) to 380 °C (Ref. 41) and for V_2AlC from 750 °C (Ref. 44) to 500 °C.[42] During HPPMS, voltages <500 V and peak currents of several A cm^{-2} are applied to the target over 20–500 μs long pulses at duty cycles <10%, which results in peak power densities of up to several kW cm^{-2}.[45] Within the pulse on-time (t_{on}), the plasma density can be increased significantly[46] which results in a higher ionization fraction of sputtered film forming species.[47,48] Ionization fractions of 70% and 40% have been measured for Cu and $Ti_{0.5}Al_{0.5}$, respectively.[47,49] The ionization fraction of film forming species is reported to be much larger than the percentage level in DCMS[50] enhancing the surface mobility of adatoms[42,51] at the growing film surface.[41] Enhanced surface diffusion may facilitate growth of high temperature phases at lower temperatures.[41,42,45,51] Hence, we utilize HPPMS to investigate the influence of the substrate temperature on the structural evolution of boron rich Al-Y-B thin films. Special attention is paid to the potential formation of competing binary phases and phases that may form as a result of impurity incorporation. Based on a correlative theoretical and experimental approach, the formation of $(Y,Al)B_6$ as a possible competing phase differing only by 1.8 at. % in boron concentration to the $AlYB_{14}$ phase is investigated.

II. EXPERIMENTAL DETAILS

The Al-Y-B films were synthesized in a high vacuum system with a base pressure of 3×10^{-5} Pa by HPPMS

utilizing a stoichiometric $AlYB_{14}$ (purity 99.9%) compound target with a diameter of 50 mm. The deposition was carried out at an Ar (99.9999% purity) pressure of 0.9 Pa. The time-averaged power density supplied by a Melec power supply (SIPP2000USB-10-500-S) was 7.1 W cm^{-2}. The pulse on-time, t_{on}, was 100 μs and the pulse off-time, t_{off}, was 2900 μs which corresponds to frequencies of 333 Hz and a duty cycle, $t_{on}/(t_{on}+t_{off})$, of 3.3%. Thereby peak power densities of 0.3 kW cm^{-2} over the whole target and 0.9 kW cm^{-2} in the race track were obtained. The target-substrate distance was 10 cm. A 50 mm sapphire wafer with an (0001) orientation was used as substrate. The substrate temperature, T_S, was varied between 675 and 800 °C. The substrate was rotated with a constant velocity of 30 rotations per minute. Further information on the deposition system can be found elsewhere.[52]

To study the film constitution and grain size distribution, XRD using a Bruker AXS D8 Discover General Area Detection Diffraction System and high resolution transmission electron microscopy (HRTEM) with SAED utilizing an FEI Titan 50–300 PICO with Cs-Cc corrector were performed. XRD measurements were carried out employing Cu K_α radiation at a fixed incidence angle of 15° using a collimator with a diameter of 0.5 mm. A 2θ-range of 15°–75° was covered during the detector scan using a 2D area detector. The chemical composition was determined by energy dispersive X-ray (EDX) analysis with an EDAX Genesis 2000 analyzer and Time-Of-Flight Elastic Recoil Detection Analysis (TOF-ERDA). The experimental details of the TOF-ERDA measurements can be found in Ref. 53 whereas the detection system and associated systematic uncertainties are discussed in a study by Zhang *et al.*[54] The sample for TEM investigation was fabricated with a focused ion beam (FIB, FEI Helios 660) followed by a post thinning-process under illumination of 500 eV ion beam (Nanomil, Fischione). Furthermore to investigate the elemental and chemical structure of the thin film EDX spectroscopy mapping as well as electron energy loss spectroscopy spectrum imaging (EELS-SI) of the samples was acquired by analytical scanning TEM (STEM, FEI Titan^3 60–300, equipped with a Super-X EDX detector and a Dual-EELS Quantum ERS GIF).

III. COMPUTATIONAL DETAILS

Density functional theory (DFT)[55] calculations were performed with the Vienna *ab initio* simulation package (VASP)[56] to determine the energy of formation of the $(Al,Y)_{2-x}B_{14}$ (x = 0, 0.25, 0.5) and $(Y,Al)_{1-y}B_6$ (y = 0, 0.0625, 0.125) systems. For the calculations generalized-gradient approximation with projector augmented wave (PAW)[57] potential, a reciprocal space integration using the Monkhorst-Pack scheme[58] and tetrahedron method for total energy using Blöchl-corrections[59] were employed. The energy cut off and the electronic relaxation convergence were 500 eV and 0.01 meV, respectively. The used k-point grids were 5 × 5 × 5 for the $(Al,Y)_{2-x}B_{14}$ and 4 × 6 × 6 for $(Y,Al)_{1-y}B_6$, for which a 4 × 2 × 2 super cell was used. The Al and Y atoms in $(Y,Al)_{1-y}B_6$ were randomly distributed on an ad hoc basis. Prior to the energy calculations, the atom positions were relaxed with a force convergence of 1 meV/Å.

Subsequently, the energy of formation was calculated using

$$E_f = \frac{\sum_i \nu_i E_i}{n_{atom}},$$

where E_f is the energy of formation per atom, ν_i the stoichiometric coefficient (negative for reactants, positive for products), E_i the energy of the specific compounds (face centered cubic Al, hexagonal Y, rhombohedric B), and n_{atom} the number of atoms in the calculated system.

IV. RESULTS AND DISCUSSION

A. Chemical composition

The sample deposited at 800 °C was measured by TOF-ERDA and used as a standard for the EDX measurements. According to the analysis performed with the CONTES program package[60] the film is found to be composed of 3.3 at. % Al, 6.7 at. % Y, 84.8 at. % B, 2.2 at. % O, and 1.6 at. % C. Impurities of F, N, Ar, and H were lower than 1 at. %. The O-content is probably caused by the incorporation of oxygen stemming from residual gas during thin film growth.[36] A local enrichment of oxygen at the film surface may be caused by subsequent exposure of the as-grown film to air.[61,62] The composition of the films deposited at lower T_S, 750–675 °C, was measured by EDX with an acceleration voltage of 6 kV using a sample quantified by ERDA as standard. The significant difference to the sample deposited at $T_S = 800$ °C is an increased Al content of 4.8 at. %. The lower Al content at $T_S = 800$ °C can be explained by the Al melting point, which is the lowest among the film constituents. Hence, preferential evaporation of Al takes place at elevated temperatures leading to these low Al-contents. The resulting Al/Y ratio of 0.57 for $T_S = 800$ °C is consistent with the composition employed in calculations reported by Kölpin *et al.*,[18] where the lowest energy of formation for the Al-Y-B system was reported for an Al/Y ratio of 0.5.[18] As the B icosahedra are electron deficient,[1] additional charge is required to stabilize the structure.[18] The phase stability therefore depends crucially on the charge transferred from the metals, e.g., Al and Y, to the boron icosahedra.[18,63,64]

B. Structure

The diffractograms of the films for T_S between 675 °C and 800 °C are shown in Fig. 3. With increasing substrate temperature the full width at half maximum decreases by 60% and 53% for peak (I) and (II), respectively, and hence the crystal quality improves. These peaks can clearly be observed at 30.76° (I) and 37.87° (II). All peak positions of the aforementioned peaks fit very well to the $AlYB_{14}$-structure as well as to the binary cubic YB_6-structure. Other phases, which could have developed due to impurities, such as AlB_{12},[34] AlB_{10},[35] AlB_2,[65] Y,[66] $YAlO_3$,[40] Y_2O_3,[39] Y_3BO_6,[67] YBO_3,[68] B_2O_3,[69] YB_{66},[70] YB_{12},[32] YB_4,[71] and YB_2,[72] have been considered as potential phases, but did not

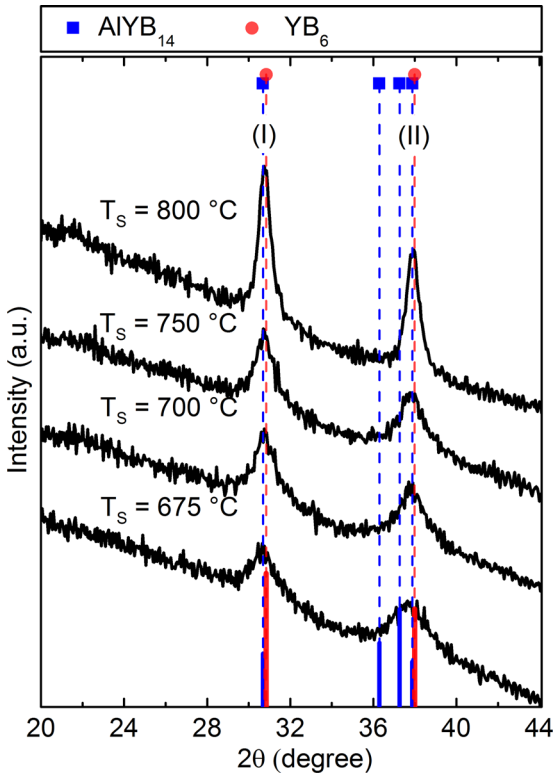

FIG. 3. XRD data of four Al-Y-B thin films deposited at 800 °C, 750 °C, 700 °C, and 675 °C. The vertical lines marked with squares represent selected peaks of $Al_{0.71}Y_{0.62}B_{14}$ based on the data of Korsukova *et al.*[16] and vertical lines marked with circles represent selected peaks of YB_6 based on the data of Blum and Bertaut.[33]

match the diffractograms and are therefore excluded from further discussions.

Based on the data of Korsukova *et al.*[16] $AlYB_{14}$ deviates by 0.07° and 0.01° from peak (I) and (II), respectively. Deviations of YB_6 based on Blum and Bertaut[33] are 0.02° and −0.02° from peak (I) and (II), respectively. Hence, a positive phase identification cannot be conducted based on XRD.

In Fig. 4, the STEM-HAADF (high-angle annular dark-field imaging) image as well as the STEM-EELS data of the Al-Y-B thin film grown at a substrate temperature of 800 °C is shown. From the STEM-HAADF image depicted in Fig. 4(a), it is evident that a nanocomposite containing nm sized crystals in an amorphous matrix is formed. To identify which crystalline phases do in fact form, energy dispersive X-ray spectroscopy mapping as well as EELS-SI correlative electron microscopy was conducted on the sample synthesized at $T_S = 800$ °C. To address the elemental distribution, EDX spectroscopy mapping was performed at high magnification (not shown here). The distribution of B is found to be uniform. Regions that lack the presence of either Y or Al completely could not be identified. Hence, all phases appear to contain B, Al, and Y. However, due to projection effects, one cannot conclude unequivocally that all phases formed do in fact contain all three alloy constituents.

EELS spectrum image (SI) was utilized to further investigate the spatial distribution of the chemical composition of the crystals. In Fig. 4(a) the dashed rectangle indicates the area in which an EELS was recorded. Simultaneous with the SI, a (low resolution) HAADF-STEM signal was recorded for relating the SI details to the microstructural features and is shown in Fig. 4(b). Indicated in Fig. 4(b) are the areas used for averaging spectra from the bright particles and the darker (less dense) matrix, and the resulting spectra are found in Fig. 4(c). Throughout the spectra, all three elements (Y, Al, and B) are present. While the fine structure of the Y and B edges (Y-M at 165 eV and B-K at 201 eV energy loss) remains largely unchanged, the Al-L edge (at ∼73 eV energy loss) is shown in detail. In Fig. 4(c), the averaged spectra originating from the crystals and the matrix are displayed. As it can be seen, there is a significant difference in the sharpness and height of the initial Al peak at ∼78 eV energy loss. The peak stemming from the crystalline region is sharper and larger in intensity (independent of crystal orientation) as compared to the amorphous matrix, indicating a different chemical environment for Al and revealing that Al exists in both crystalline particles and amorphous matrix. While two distinctly different signals are observed from this region, the underlying edge profile is rather similar. It should be noted that EELS at this nanometer scale and at these energy losses is not entirely straightforward. Initially,

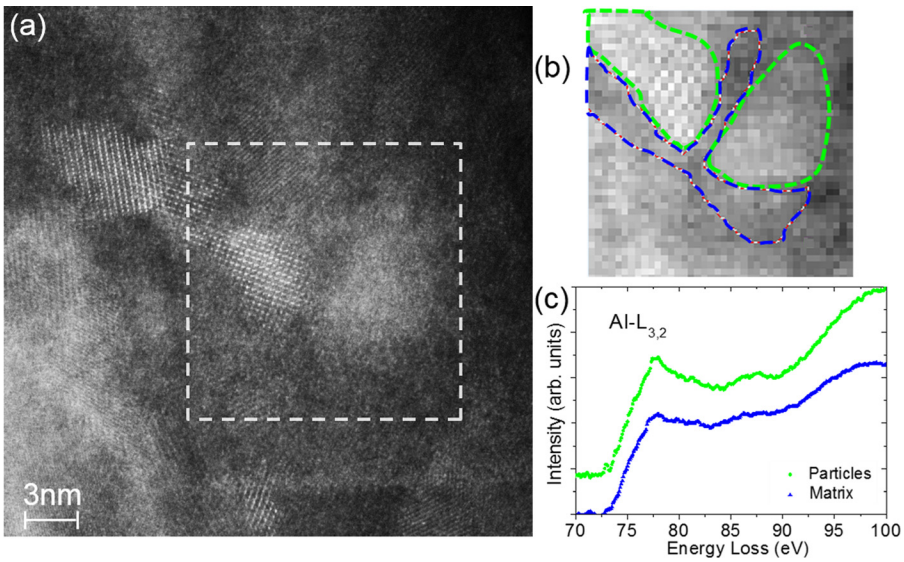

FIG. 4. (a) STEM-HAADF image of Al-Y-B thin film at a substrate temperature of 800 °C: bright crystals percolated by darker surrounding area (b) indicated areas used for averaging the spectra from bright crystals and darker matrix (c) STEM-EELS normalized to the area underneath the curves. For better presentation, the EELS spectra are shifted laterally. Both particle and matrix data start with zero intensity.

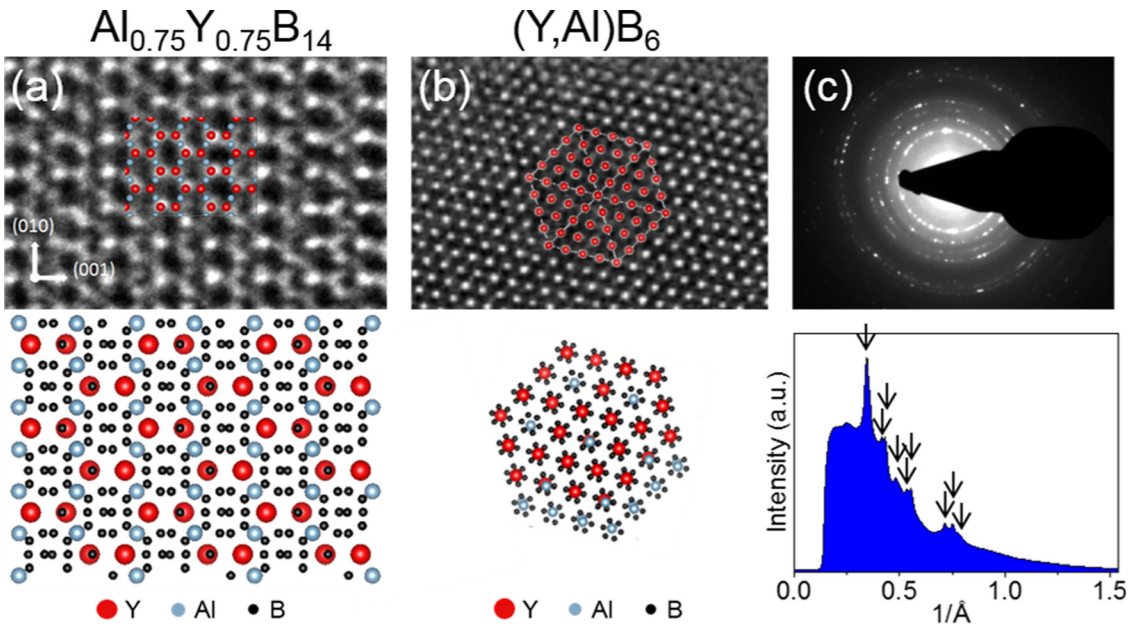

FIG. 5. HRTEM images: (a) left: top $AlYB_{14}$ crystal, (100) orientation, bottom: $AlYB_{14}$ structure from calculations; (b) middle: top: $(Y,Al)B_6$ crystal, (111) orientation, bottom: $(Y,Al)B_6$ structure from calculations; (c) right: top: SAED data from $AlYB_{14}$ film deposited at 800 °C; bottom: resulting spectrum of rotational average, arrows indicate the peaks used for d-spacing calculation.

geometrical considerations must be taken into account, such as the converging (~20 mrad half angle) passing through a sample of limited thickness, with potential overlap of multiple particles and embedding matrix in the projected direction. To minimize overlap, the data were recorded at the thin edge of the sample, where it is possible to distinguish and exclude regions with overlapping crystals. Additionally, in these thin regions the Å-sized converging beam is not exciting the matrix and crystal other than at the interface. Additionally, core-loss EELS is a delocalized method such that information is acquired outside of the beam with exponentially reduced probability. Typically, for Al-L losses, the spectrum is acquired from less than a nm from the beam and this causes a mixing of both crystal and matrix components. However, the average spectrum acquired on the crystal exhibits the more crystal like component, while the matrix component dominates in the average matrix spectrum.

This supports strongly the notion that the peaks observed by XRD originate from crystals forming a ternary phase, and not from a potentially competing binary phase, embedded in an amorphous matrix containing Al, Y, and B. Furthermore, the trend that more Y is located in the crystalline areas is consistent with both the formation of $AlYB_{14}$ or $(Y,Al)B_6$: based on systematic DFT study of the occupancies of Al and Y in $Al_xY_yB_{14}$ the most stable phase predicted is $Al_{0.5}YB_{14}$.[18]

To determine which ternary boride is formed HRTEM has been carried out on the crystalline areas. The formation of two different phases is evident. The two different crystal systems are illustrated in the lower part of Figs. 5(a) and 5(b). Fig. 5(a): The orthorhombic $AlYB_{14}$ (space group: *Imma*) containing boron-icosahedra with five-fold symmetry and (b) $(Y,Al)B_6$ with its body-centered cubic symmetry (bcc) structure are revealed. In Figs. 5(a) and 5(b), both structures are compared to structural data obtained from quantum mechanical calculations. For illustrative purposes, the boron atoms have been left out in both images as they are undetectable in HRTEM due to the high density (87.5 at. %) and therefore small inter-spacing between boron atoms, which result in a very low contrast for the lattice image. The HRTEM data shown in Fig. 5(a) are consistent with the theoretic model in (100) orientation, clearly indicating the phase formation of the orthorhombic $AlYB_{14}$. This notion is also corroborated by SAED data shown in Fig. 5(c). The aperture size was approximately 300 nm; therefore based on the STEM-HAADF image in Figs. 4(a) and 4(b), it is expected that diffraction data stem from the whole nanocomposite. The diffuse ring in the SAED data indicates the presence of an amorphous phase which is also consisted with the STEM-HAADF image shown in Fig. 4(a). 9 diffraction rings can be observed and are shown as isolated peaks in the diffractogram in Fig. 5(c) by a rotational average-approach.[73] The diffractogram was calibrated against polycrystalline gold nanoparticles using the same camera length. The corresponding reciprocal values of d-spacings are marked with arrows in Fig. 5(c) bottom. The d-spacings are listed in Table I. It is evident that the most pronounced diffracted intensity stems from the first two rings. To compare the SAED results with the XRD and JCPDS data, these are summarized in Table I.

d-Spacings according to SAED and XRD as well as the (hkl) and diffraction data of YB_6[33] and $Al_{0.71}Y_{0.62}B_{14}$[16] are listed in Table I. Additionally, the deviations between SAED and the diffraction data are given. Six SAED rings are assigned to either YB_6[33] or $AlYB_{14}$[16] with a maximum deviation of 0.44% between the JCPDS data and the experimentally determined lattice spacings, see bold marked lines. $d_{SAED} = 2.316$ Å might be assigned to B_2O_3[69] whereby $d_{SAED} = 1.872$ and 1.806 Å might be assigned to Y_2O_3.[39] Hence these diffraction rings are assumed to originate from oxide formation which is consistent with the chemical

TABLE I. Comparison of d-spacing of SAED data with diffraction data of YB_6[33] and $Al_{0.71}Y_{0.62}B_{14}$,[16] as well as the d-spacing according to the XRD peaks are shown. Additionally, the deviations Δ (%) are shown for possible oxides B_2O_3[69] and Y_2O_3.[39] d-Spacings which can be assigned to YB_6[33] or $Al_{0.71}Y_{0.62}B_{14}$[16] are marked in bold.

	YB_6[33]			$Al_{0.71}Y_{0.62}B_{14}$[16]				
SAED (Å)	hkl	d (Å)	Δ (%)	hkl	d (Å)	Δ (%)	Other phases Δ (%)	XRD (Å)
2.896	**110**	**2.908**	**0.42**	200	2.911	0.50		2.907
2.403	111	2.375	−1.21	**132**	**2.411**	**0.31**		2.376
2.316				141	2.282	−1.47	B_2O_3[69]:−0.42	
2.064	**200**	**2.057**	**−0.36**	004	2.049	−0.75		
1.872	210	1.839	−1.79	301	1.888	0.84	Y_2O_3[39]:0.08	
1.806				143	1.793	−0.73	Y_2O_3[39]:0.66	
1.399	300	1.371	−2.06	**420**	**1.402**	**0.17**		
1.332				**422**	**1.326**	**−0.44**		
1.289	310	1.301	0.88	**055**	**1.288**	**−0.10**		

composition data discussed above or due to post-oxidation of the TEM sample. For lower d spacing values, more peaks could be assigned but as the data quality decreases, as shown in Fig. 5(c), these diffraction rings are not discussed further as the difference between peak position and JCPDS data are smaller than the measurement error of the SAED. In summary, the SAED data confirm the HRTEM regarding the phase formation as the diffraction data clearly show the formation of both here discussed boride phases: $AlYB_{14}$[16] as well as YB_6.[33]

C. Calculations

The above identified ternary hexaboride phase $(Y,Al)B_6$ (see Figs. 5(b) and 5(c) as well as Table I) has been investigated by DFT. As discussed above, growth of $AlYB_{14}$[10,16,18] is challenging. $(Y,Al)_{1-y}B_6$ (y = 0, 0.0625, 0.125) is considered as a potential competing phase for this ternary system at high B contents. YB_6 exhibits a body-centered cubic phase.[33] In this work, calculations have been performed pertaining to the formation of a solid solution where Y is partly substituted by Al, while metal vacancies are introduced in order to study higher boron contents. It should be noted that the Y-B phase diagram suggests significant solubility of vacancies on the metal sublattice of YB_6.[74] Energy of formation data for $(Al,Y)_{2-x}B_{14}$ (x = 0, 0.25, 0.5) and $(Al,Y)_{1-y}B_6$ (y = 0, 0.0625, 0.125) has been calculated and is shown in Fig. 6. Al/Y ratio is kept constant at 1. According to the energy formation data, the stability range for $(Al,Y)_{2-x}B_{14}$ (x = 0, 0.25, 0.5) extends from a boron to metal ratio of 14–6.4, while for a metal to boron ratio of smaller than 6.4 the cubic $(Y,Al)_{1-y}B_6$ (y = 0, 0.0625, 0.125) phase appears to be stable. The required high vacancy concentration on metal sublattices leads to multiple feasible arrangements of metal atoms. Hence, considering possible variations in energy deviations were estimated to be ±10% and are shown in Fig. 6. These estimations are consistent with the literature for $AlYB_{14}$.[18] Additionally, the target composition and the composition of the film deposited at 800 °C are shown in Fig. 6. From these data, it is evident that fluctuations in film composition may cause the formation of thin films containing both the $(Al,Y)_{2-x}B_{14}$ phase and the cubic $(Y,Al)_{1-y}B_6$ phase. It may be speculated that the composition modulation is caused by the competitive nucleation of phases with different solubility for the sputtered elements and or by the formation of impurity phases such as oxides modifying the local composition. Both scenarios are expected to result in the formation of the here observed nanocomposite structure.

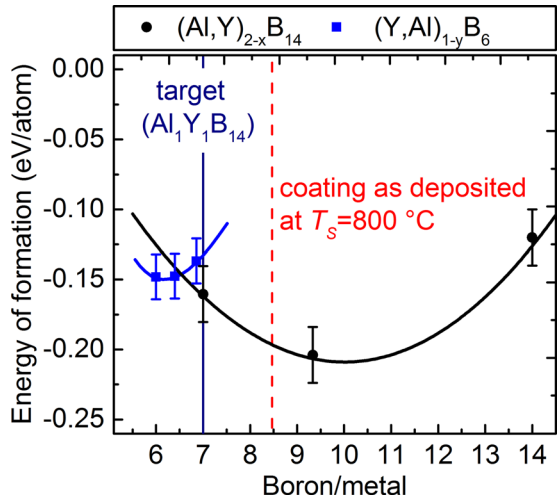

FIG. 6. Energy of formation as a function of boron/metal ratio of $(Al,Y)_{2-x}B_{14}$ (x = 0, 0.25, 0.5) and $(Y,Al)_{1-y}B_6$ (y = 0, 0.0625, 0.125). Additionally, the boron/metal ratio of the target and the coating as deposited at T_S = 800 °C is given. The energy of formation data was fitted by cubic functions and provided as a guide for the eye.

V. CONCLUSIONS

The phase formation in boron-rich section of the Al-Y-B system has been explored by a correlative theoretical and experimental research strategy. Correlative structure and bonding analysis indicate that the crystals formed in the amorphous matrix are icosahedrally bonded $AlYB_{14}$ and cubic $(Y,Al)B_6$. HRTEM and SAED data allow the phase identification of coexisting of icosahedrally bonded $AlYB_{14}$ and cubic $(Y,Al)B_6$. Based on quantum mechanical calculations, we infer that minute composition variations within the film may be responsible for the formation of both icosahedrally bonded $AlYB_{14}$ and cubic $(Y,Al)B_6$ phases. These findings are relevant for synthesis attempts of all boron-rich icosahedrally bonded compounds with the space group: *Imma* that form ternary phases at similar compositions.

ACKNOWLEDGMENTS

This research was supported by the Deutsche Forschungsgemeinschaft within the Collaborative Research Center SFB-TR 87/2 "Pulsed high power plasmas for the synthesis of nanostructured functional layers." Simulations were performed with computing resources granted by JARA-HPC from RWTH Aachen University under Project No. JARA0131. P.O.Å.P. wishes to acknowledge the Knut and Alice Wallenberg Foundation for support of the electron microscopy laboratory in Linköping.

[1]D. Emin, Phys. Today **40**(1), 55 (1987).
[2]V. Domnich, S. Reynaud, R. A. Haber, and M. Chhowalla, J. Am. Ceram. Soc. **94**, 3605 (2011).
[3]J. E. Lowther, Physica B **322**(1–2), 173 (2002).
[4]A. M. Grishin, S. I. Khartsev, J. Böhlmark, and M. Ahlgren, JETP Lett. **100**, 680 (2015).
[5]C. Higdon, B. Cook, J. Harringa, A. Russell, J. Goldsmith, J. Qu, and P. Blau, Wear **271**, 2111 (2011).
[6]H. Kölpin, D. Music, G. Henkelman, and J. M. Schneider, Phys. Rev. B **78**, 054122 (2008).
[7]Y. Lee and B. N. Harmon, J. Alloys Compd. **338**, 242 (2002).
[8]B. A. Cook, J. L. Harringa, T. L. Lewis, and A. M. Russell, Scr. Mater. **42**, 597 (2000).
[9]D. Emin, J. Solid State Chem. **179**, 2791 (2006).
[10]S. Maruyama, Y. Miyazaki, K. Hayashi, T. Kajitani, and T. Mori, Appl. Phys. Lett. **101**, 152101 (2012).
[11]S. Maruyama, A. Prytuliak, Y. Miyazaki, K. Hayashi, T. Kajitani, and T. Mori, J. Appl. Phys. **115**, 123702 (2014).
[12]H. Hubert, B. Devouard, and L. A. J. Garvie, Nature **391**, 376 (1998).
[13]P. A. Molian and M. Womack, U.S. patent 2003/0219605 A1 (27 November 2003).
[14]L. A. J. Garvie and H. Hubert, J. Solid State Chem. **133**, 365 (1997).
[15]Y. Tian, A. Constant, C. C. H. Lo, J. W. Anderegg, A. M. Russell, J. E. Snyder, and P. Molian, J. Vac. Sci. Technol., A **21**, 1055 (2003).
[16]M. M. Korsukova, T. Lundström, and L.-E. Tergenius, J. Alloys Compd. **187**, 39 (1992).
[17]I. Higashi, M. Kobayashi, S. Okada, K. Hamano, and T. Lundström, J. Cryst. Growth **128**, 1113 (1993).
[18]H. Kölpin, D. Music, G. Henkelman, J. Emmerlich, F. Munnik, and J. M. Schneider, J. Phys.: Condens. Matter **21**, 355006 (2009).
[19]V. I. Matkovich and J. Economy, Acta Crystallogr., Sect. B: Struct. Crystallogr. Cryst. Chem. **26**, 616 (1970).
[20]K. Kudou, S. Okada, T. Mori, K. Iizumi, T. Shishido, T. Tanaka, I. Higashi, K. Nakajima, P. Rogl, Y. B. Andersson, and T. Lundström, Jpn. J. Appl. Phys., Part 2 **41**, L928 (2002).
[21]S. Okada, T. Tanaka, A. Sato, T. Shishido, K. Kudou, K. Nakajima, and T. Lundström, J. Alloys Compd. **395**, 231 (2005).
[22]A. Guette, M. Barret, R. Naslain, and P. Hagenmuller, J. Less Common Metals **82**, 325 (1981).
[23]M. M. Korsukova, Phys. Status Solidi **114**, 265 (1989).
[24]Y. Lei, Q.-S. Meng, L. Zhuang, S. Chen, L. Hu, and H. Cheng, Tribol. Lett. **56**, 435 (2014).
[25]Y. Lei, Q.-S. Meng, L. Zhuang, S.-P. Chen, and J.-J. Dai, Appl. Surf. Sci. **347**, 155 (2015).
[26]Z. Wu, Y. Bai, W. Qu, A. Wu, D. Zhang, J. Zhao, and X. Jiang, Vacuum **85**, 541 (2010).
[27]C. Yan, S. K. Jha, J. C. Qian, Z. F. Zhou, B. He, T. W. Ng, K. Y. Li, W. J. Zhang, I. Bello, J. E. Klemberg-Sapieha, and L. Martinu, Appl. Phys. Lett. **102**, 122110 (2013).
[28]C. Yan, J. C. Qian, T. W. Ng, Z. F. Zhou, K. Y. Li, W. J. Zhang, I. Bello, L. Martinu, and J. E. Klemberg-Sapieha, Surf. Coat. Technol. **232**, 535 (2013).
[29]Joint Committee on Powder Diffraction Standards (JCPDS), International Centre for Diffraction Data, Newtown Square, PA, USA, Card No. 75–1262.
[30]S. Mráz, J. Emmerlich, F. Weyand, and J. M. Schneider, J. Phys. D: Appl. Phys. **46**, 135501 (2013).
[31]J. Neidhardt, S. Mráz, J. M. Schneider, E. Strub, W. Bohne, B. Liedke, W. Möller, and C. Mitterer, J. Appl. Phys. **104**, 063304 (2008).
[32]Joint Committee on Powder Diffraction Standards (JCPDS), International Centre for Diffraction Data, Newtown Square, PA, USA, Card No. 73–1382.
[33]P. P. Blum and F. Bertaut, Acta Crystallogr. **7**, 81 (1954).
[34]Joint Committee on Powder Diffraction Standards (JCPDS), International Centre for Diffraction Data, Newtown Square, PA, USA, Card No. 12–0639.
[35]Joint Committee on Powder Diffraction Standards (JCPDS), International Centre for Diffraction Data, Newtown Square, PA, USA, Card No. 15–0617.
[36]J. M. Schneider, B. Hjörvarsson, X. Wang, and L. Hultman, Appl. Phys. Lett. **75**, 3476 (1999).
[37]D. Music and J. M. Schneider, New J. Phys. **15**, 073004 (2013).
[38]Joint Committee on Powder Diffraction Standards (JCPDS), International Centre for Diffraction Data, Newtown Square, PA, USA, Card No. 46–1212.
[39]Joint Committee on Powder Diffraction Standards (JCPDS), International Centre for Diffraction Data, Newtown Square, PA, USA, Card No. 41–1105.
[40]Joint Committee on Powder Diffraction Standards (JCPDS), International Centre for Diffraction Data, Newtown Square, PA, USA, Card No. 38–0222.
[41]H. Bolvardi, J. Emmerlich, S. Mráz, M. Arndt, H. Rudigier, and J. M. Schneider, Thin Solid Films **542**, 5 (2013).
[42]Y. Jiang, S. Mráz, and J. M. Schneider, Thin Solid Films **538**, 1 (2013).
[43]J. Emmerlich, D. Music, M. Braun, P. Fayek, F. Munnik, and J. M. Schneider, J. Phys. D: Appl. Phys. **42**, 185406 (2009).
[44]D. P. Sigumonrong, J. Zhang, Y. Zhou, D. Music, and J. M. Schneider, J. Phys. D: Appl. Phys. **42**, 185408 (2009).
[45]K. Sarakinos, J. Alami, and S. Konstantinidis, Surf. Coat. Technol. **204**, 1661 (2010).
[46]M. Lattemann, U. Helmersson, and J. E. Greene, Thin Solid Films **518**, 5978 (2010).
[47]V. Kouznetsov, K. Macák, J. M. Schneider, U. Helmerson, and I. Petrov, Surf. Coat. Technol. **122**, 290 (1999).
[48]U. Helmersson, M. Lattemann, J. Bohlmark, A. Ehiasarian, and J. T. Gudmundsson, Thin Solid Films **513**, 1 (2006).
[49]K. Macák, V. Kouznetsov, J. M. Schneider, and U. Helmerson, J. Vac. Sci. Technol., A **18**, 1533 (2000).
[50]I. Petrov, A. Myers, J. E. Greene, and J. R. Abelson, J. Vac. Sci. Technol., A **12**, 2846 (1994).
[51]I. Petrov, P. B. Barna, L. Hultman, and J. E. Greene, J. Vac. Sci. Technol. **21**, S117 (2003).
[52]S. Reeh, D. Music, T. Gebhardt, M. Kasprzak, T. Jäpel, S. Zaefferer, D. Raabe, S. Richter, A. Schwedt, J. Mayer, B. Wietbrock, G. Hirt, and J. M. Schneider, Acta Mater. **60**, 6025 (2012).
[53]M. Hans, M. to Baben, D. Music, J. Ebenhöch, D. Primetzhofer, D. Kurapov, M. Arndt, H. Rudigier, and J. M. Schneider, J. Appl. Phys. **116**, 093515 (2014).
[54]Y. Zhang, H. J. Whitlow, T. Winzell, I. F. Bubb, T. Sajabaara, K. Arstila, and J. Keinonen, Nucl. Instrum. Methods Phys. Res., Sect. B **149**, 477 (1999).
[55]P. Hohenberg and W. Kohn, Phys. Rev. **136**, B864 (1964).
[56]G. Kresse and J. Hafner, Phys. Rev. B **49**, 14251 (1994).
[57]G. Kresse and D. Joubert, Phys. Rev. B **59**, 1758 (1999).
[58]H. J. Monkhorst and J. D. Pack, Phys. Rev. B **13**, 5188 (1976).
[59]P. E. Blöchl, O. Jepsen, and O. K. Andersen, Phys. Rev. B **49**, 16223 (1994).
[60]M. S. Janson, CONTES Instruction Manual Uppsala, Internal Report (2004).
[61]C. Kunze, D. Music, M. To Baben, J. M. Schneider, and G. Grundmeier, Appl. Surf. Sci. **290**, 504 (2014).
[62]C. Gnoth, C. Kunze, M. Hans, M. to Baben, J. Emmerlich, J. M. Schneider, and G. Grundmeier, J. Phys. D: Appl. Phys. **46**, 084003 (2013).
[63]L. F. Wan and S. P. Beckman, Mater. Lett. **74**, 5 (2012).
[64]J. Emmerlich, N. Thieme, M. to Baben, D. Music, and J. M. Schneider, J. Phys.: Condens. Matter **25**, 335501 (2013).
[65]Joint Committee on Powder Diffraction Standards (JCPDS), International Centre for Diffraction Data, Newtown Square, PA, USA, Card No. 39–1483.
[66]Joint Committee on Powder Diffraction Standards (JCPDS), International Centre for Diffraction Data, Newtown Square, PA, USA, Card No. 33–1458.
[67]Joint Committee on Powder Diffraction Standards (JCPDS), International Centre for Diffraction Data, Newtown Square, PA, USA, Card No. 34–0291.
[68]Joint Committee on Powder Diffraction Standards (JCPDS), International Centre for Diffraction Data, Newtown Square, PA, USA, Card No. 74–1929.
[69]Joint Committee on Powder Diffraction Standards (JCPDS), International Centre for Diffraction Data, Newtown Square, PA, USA, Card No. 41–0626.
[70]Joint Committee on Powder Diffraction Standards (JCPDS), International Centre for Diffraction Data, Newtown Square, PA, USA, Card No. 24–1417.
[71]Joint Committee on Powder Diffraction Standards (JCPDS), International Centre for Diffraction Data, Newtown Square, PA, USA, Card No. 74–1069.
[72]Joint Committee on Powder Diffraction Standards (JCPDS), International Centre for Diffraction Data, Newtown Square, PA, USA, Card No. 25–1032.
[73]D. R. G. Mitchell, Microsc. Res. Tech. **71**, 588 (2008).
[74]P. K. Liao and K. E. Spear, J. Phase Equilib. **16**, 521 (1995).